HEIGHTS initial simulation of discharge produced plasma hydrodynamics and radiation transport for extreme ultraviolet lithography

A. Hassanein
V. Sizyuk
V. Tolkach
V. Morozov
Argonne National Laboratory
Argonne, Illinois 60439
E-mail: hassanien@anl.gov

B. Rice
Intel Corporation
Component Research Division
Hillsboro, Oregon 97124

Abstract. Discharge-produced plasma (DPP) devices have been proposed as a light source for EUV lithography. A key challenge for DPP is achieving sufficient brightness to support the throughput requirements of exposure tools for high-volume manufacturing lithography. To simulate the environment of the EUV source and optimize the output of the source, an integrated model is being developed to describe the hydrodynamic and optical processes that occur in DPP devices. The model includes both plasma evolution and magnetohydrodynamic processes as well as detailed photon radiation transport. The total variation diminishing scheme in the Lax-Friedrich formulation for the description of magnetic compression and diffusion in a cylindrical geometry is used. Several models are being developed for opacity calculations: a collisional radiation equilibrium model, a self-consistent field model with Auger processes, and a nonstationary kinetic model. Radiation transport for both continuum and lines with detailed spectral profiles are taken into account. The developed models are integrated into the HEIGHTS-EUV computer simulation package. Preliminary results of a numerical simulation of xenon gas hydrodynamics and EUV radiation output are presented for various plasma conditions. [DOI: 10.1117/1.1631445]

Subject terms: Discharge-produced plasma; HEIGHTS-EUV; magnetohydrodynamics; radiation transport; numerical simulation.

Paper 03023 received Mar. 4, 2003; revised manuscript received Jun. 19, 2003; accepted for publication Jul. 22, 2003.

1 Introduction

This paper presents an integrated model that is being developed to describe the hydrodynamics and optical processes that occur in discharge-produced plasma (DPP) devices. The model will eventually address three main subjects: plasma evolution and magnetohydrodynamic (MHD) processes, detailed photon radiation transport, and interaction between plasma/radiation and material. Regions with differing propagation speeds of perturbation require accurate numerical solutions of the MHD equations. The total variation diminishing (TVD) scheme in the Lax-Friedrich formulation for the description of magnetic compression and diffusion in a cylindrical multidimensional geometry is the most suitable and is used in our model. Several models are being developed and can be used to calculate opacity data: a collisional radiation equilibrium (CRE) model, which is a self-consistent model that takes into account Auger processes, and a nonstationary kinetic model that depends on the complexity of the problem and the availability of computer time. Radiation transport for both continuum and lines with detailed spectral profiles are being taken into account. The developed models are integrated into the HEIGHTS-EUV computer simulation package. The package can also be used to study the hydrodynamics and radiation of two-gas mixtures in dense plasma focus (DPF) devices in the presence of impurities and erosion products that can affect radiation output.

The goal of this paper is to provide our initial simulation of MHD and optical processes that occur in DPP devices of standard Mather-type electrode construction. Such a device is schematically shown in Fig. 1. The electrodes are shown in dark color and are of equal height. The device is filled by xenon gas under an initial pressure in the range of several tens of mtorr at room temperature, corresponding to an initial density of the gas in the range of 10^{14} to 10^{15} cm^{-3}. It is also assumed that a preionization step that heats the gas to a temperature of $\approx$1 eV occurs near the bottom of the device.

2 Mathematical Model

We solve the general set of three-dimensional (3-D) resistive conservative MHD equations[1] that contain the description of the behavior of conductive flow in the magnetic field due to current displacement triggered by the discharge. The processes of all magnetic diffusion and radiation energy loss are included.

$$\frac{\partial \rho}{\partial t} + \nabla \cdot (\rho \mathbf{v}) = 0, \tag{1}$$

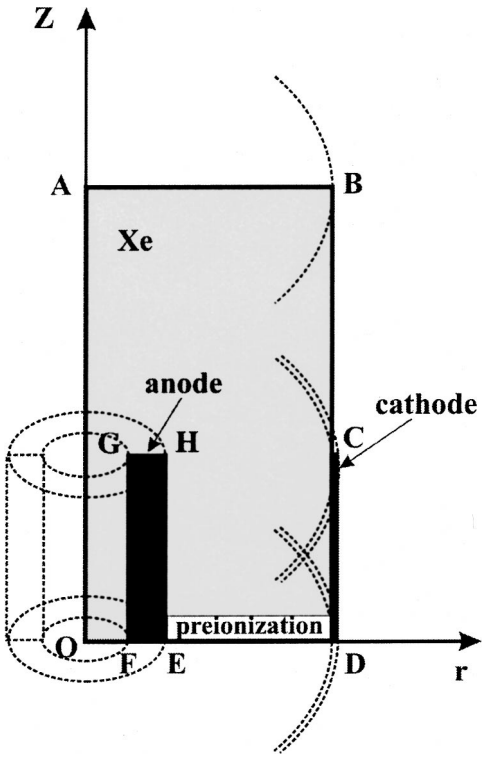

Fig. 1 Schematic view of a DPF device.

$$\frac{\partial \rho \mathbf{v}}{\partial t} + \nabla \cdot \left(\rho \mathbf{v}\mathbf{v} + p_{\text{tot}} - \frac{1}{4\pi}\mathbf{B}\mathbf{B} \right) = 0, \tag{2}$$

$$\frac{\partial e_{\text{tot}}}{\partial t} + \nabla \cdot \left[\mathbf{v}(e_{\text{tot}} + p_{\text{tot}}) - \frac{1}{4\pi}(\mathbf{v}\cdot\mathbf{B})\mathbf{B} + \frac{c^2\eta}{16\pi^2}(\nabla \times \mathbf{B}) \times \mathbf{B} - \chi \nabla T - \mathbf{S}_{\text{rad}} \right] = 0, \tag{3}$$

$$\frac{\partial \mathbf{B}}{\partial t} + \nabla \cdot (\mathbf{v}\mathbf{B} - \mathbf{B}\mathbf{v}) + \frac{c^2}{4\pi}\nabla \times (\eta \nabla \times \mathbf{B}) = 0. \tag{4}$$

Equations (1) to (4) represent, in Gaussian units, the conservation of mass, momentum, energy, and magnetic flux, respectively. The plasma is described by the conservative variables of mass density ρ, momentum density $\rho\mathbf{v}$, total energy density e, and magnetic field $\mathbf{B}$. In the rest of the paper, the magnetic permeability $\boldsymbol{\mu}$ is assumed to be 1. Total energy density is determined as a sum of internal, kinetic, and magnetic energy densities, whereas the pressure term is separated into hydrodynamic and magnetic parts:

$$e_{\text{tot}} = e_h + \frac{\mathbf{B}^2}{8\pi} = e_{\text{int}} + \frac{\rho \mathbf{v}^2}{2} + \frac{\mathbf{B}^2}{8\pi}, \qquad p_{\text{tot}} = p_h + \frac{\mathbf{B}^2}{8\pi}. \tag{5}$$

To complete this full system of MHD equations, thermodynamic pressure $p_h = p_h(e_{\text{int}}, \rho)$, resistivity $\eta = \eta(e_{\text{int}}, \rho)$, and thermal conductivity $\chi = \chi(e_{\text{int}}, \rho)$ functions are calculated from the equation of state, discussed in the following.

Applying cylindrical symmetry of a plasma focus device, we wrote the general set of MHD Eqs. (1) to (4) in axisymmetrical cylindrical geometry (r, φ, z). We neglect the plasma motion in the φ direction and assume that magnetic field has only one component B_φ. Therefore, to simplify the expressions, subscript φ is further omitted from the magnetic field term.

In coordinate formulation, the general set can be written as

$$\frac{\partial \mathbf{U}}{\partial t} + \frac{1}{r}\frac{\partial}{\partial r}[r\mathbf{F}(\mathbf{U})] + \frac{\partial \mathbf{P}(\mathbf{U})}{\partial r} + \frac{\partial \mathbf{G}(\mathbf{U})}{\partial z} = \boldsymbol{\Omega}, \tag{6}$$

where

$$\mathbf{U} = \begin{bmatrix} \rho \\ \rho v^r \\ \rho v^z \\ e_{\text{tot}} \\ B \end{bmatrix},$$

$$\mathbf{F}(\mathbf{U}) = \begin{bmatrix} \rho v^r \\ \rho v^r v^r \\ \rho v^z v^r \\ v^r(e_{\text{tot}} + p_{\text{tot}}) - \dfrac{c^2 \eta B}{16\pi^2 r}\left[\dfrac{\partial}{\partial r}(rB)\right] - \chi \dfrac{\partial T}{\partial r} \\ 0 \end{bmatrix},$$

$$\mathbf{P}(\mathbf{U}) = \begin{bmatrix} 0 \\ p_{\text{tot}} \\ 0 \\ 0 \\ v^r B - \dfrac{c^2 \eta}{4\pi r}\dfrac{\partial rB}{\partial r} \end{bmatrix}, \tag{7}$$

$$\boldsymbol{\Omega} = \begin{bmatrix} 0 \\ -\dfrac{B^2}{4\pi r} \\ 0 \\ Q_{\text{rad}} \\ 0 \end{bmatrix},$$

$$\mathbf{G}(\mathbf{U}) = \begin{bmatrix} \rho v^z \\ \rho v^r v^z \\ \rho v^z v^z + p_{\text{tot}} \\ v^z(e_{\text{tot}} + p_{\text{tot}}) - \dfrac{c^2 \eta B}{16\pi^2}\dfrac{\partial B}{\partial z} - \chi \dfrac{\partial T}{\partial z} \\ v^z B - \dfrac{c^2 \eta}{4\pi}\dfrac{\partial B}{\partial z} \end{bmatrix},$$

and the solution of **U** entirely defines the state of the system.

The conservative form of the initial equations allows the use of the TVD method in Lax-Friederich formulation (TVD-LF) for the numerical solution of the system.[1] A second-order TVD-LF scheme can be applied to the system of conservation laws that does not use either a Riemann solver or the characteristic wave solution. Matrix formalism enables us to change the governing equations [Eqs. (6)] without significantly modifying the method. For example, to calculate a two-gas mixture approximation, it is necessary to add the second continuity equation and extend the elements of matrixes to six terms.

To calculate the radiation heat flux, the radiation transport equation[2,3] (RTE), which presents the energy conservation law for the total radiative intensity S must be solved. In this paper, we utilized the discrete-ordinates method, which varies the radiative intensity along specified directions.[4] The RTE is thus solved for a set of discrete directions that span the total spherical solid angle of 4π.

At each point of the MHD zone, local temperature T, the Plank function I_P, and optical coefficients κ_{emi} and κ_{abs} of emission and absorption of the photon with energy E define the specific intensity of radiation. In the case of axisymmetric cylindrical coordinates (r,z), the RTE for intensity I_E can be written along the direction s as

$$\frac{\mathrm{d}I_E}{\mathrm{ds}} = \sin\theta\left(\mu\frac{\partial I}{\partial r} + \frac{1-\mu^2}{r}\frac{\partial I_E}{\partial \mu}\right) + \cos\theta\frac{\partial I_E}{\partial z} = \kappa_{\text{emi}} I_P - \kappa_{\text{abs}} I_E . \tag{8}$$

Here, θ is the angle between the direction of the ray s and the z axis; φ is the angle between the projection of the direction s to the plane, perpendicular to z, and normal to the cylindrical surface; and $\mu = \cos\varphi$. The intensity in direction s is calculated by integration over all of the photon frequencies. Net flux $\mathbf{S}_{\text{rad}}$ is obtained by integrating over all of the angles:

$$\mathbf{S}_{\text{rad}} = \int\left[\int_0^{2\pi}\mathrm{d}\varphi\int_0^{\pi} I_E(\theta,\varphi)\cos\theta\sin\theta\,\mathrm{d}\theta\right]\mathrm{d}E. \tag{9}$$

The radiation energy loss in each cell is then found from $Q_{\text{rad}} = \nabla\cdot\mathbf{S}_{\text{rad}}$. Essentially, this method is the result of finite differencing of the directional dependence of the RTE. Integrals over solid angles are approximated by numerical quadrature, the choice of which defines the directions of the RTE. The solution is carried out simultaneously with the solution of energy balance to provide the distribution of the local energy source, temperature, and density profile.

The calculation of thermodynamic and optical plasma characteristics is performed in several steps, which are described in more detail in the section on atomic and opacities data.

3 Boundary Conditions

To simulate various possible effects that occur in the boundaries of the EUV source, we considered several methods of stating these effects in the form of boundary conditions. In simplified form, one can subdivide these conditions into two major parts. A hydrodynamic part includes the conditions applied to hydrodynamic flow in the area or near the boundaries. Magnetic field conditions manage the behavior of the current and the magnetic field near the surfaces of the device. In the following discussion, we refer the reader to Fig. 1.

The hydrodynamic boundary conditions are

1. *Rigid wall boundary:* $F_n|_b = 0$, where F_n is normal to the boundary component of hydrodynamic flux. Such a condition is applied at the cathode and anode surfaces $|GF|$, $|GH|$, $|HE|$, and $|CD|$ to set up the absence of flow passing through the boundary.
2. *Z-axis symmetry:* $\rho v_0^r = -\rho v_1^r$, $\rho v_{-1}^r = -\rho v_2^r$. A mirror-like condition is stated in $|OA|$ that there is no radial hydrodynamic flow on the Z axis.

The magnetic field initial and boundary conditions are

1. *Driving magnetic field:* This is applied in $|ED|$ as $B = (2I)/(cr)$, where I is the total current of the device, r is the upper radius, and c is the speed of light.
2. *Conducting solid wall without surface current:* $\partial(rB)/\partial r = 0$. This condition states that the current is concentrated at the surface of a conductor and is applied at the surface of the cathode $|CD|$ and the internal surface of the anode $|GF|$.
3. *Ideal conducting wall, total current flows at the surface:* $B = 0$. As before, this condition states that total current is concentrated at the external surface of the conductor, and is applied on the external surface of the anode $|HE|$.
4. *Z-axis symmetry:* $B|_{r=0} = 0$, $B_0 = B_1$, $B_{-1} = B_2$. The symmetry of the domain defines the symmetry of the magnetic field.

4 Atomic and Opacities Data

The results of theoretical approximations of atomic data strongly depend on the chosen theoretical models,[5–7] and, this is particularly true for high-Z materials. The atomic energy levels and radiative transition probabilities are usually calculated by modified simplifications of the Hartree-Fock (HF) method rather than by the pure HF method. One of the most widely used simplifications, suggested by Slater,[8] is known as the method of Hartree-Fock-Slater (HFS). The energy levels in HFS are calculated for the whole configurations, i.e., just one atomic level corresponds to each pair of quantum numbers (n,l), neglecting the LS splitting of nonfilled shells.

The problem is, in fact, that such shells may contain a large number of terms and levels. For example, to account for splitting each term into levels with momentum J, the d^5 shell contains 16 terms and 37 levels and the f^7 shell correspondingly contains 119 terms and 327 levels. In HFS approximation, the transition $4d^q$ to $4d^{q-1}4f$ will have just one strong line, but splitting the level will replace it into several hundreds weak lines. Knowing that transition strength is left unchanged, the radiation in strong lines may be collapsed for dense plasma, whereas the radiation in weak lines stays optically transparent. In cases when the

temperature of xenon plasma reaches 20 to 30 eV and densities are in the range of 10^{17} to 10^{18} cm^{-3}, most radiation would be concentrated in lines, and so, line splitting may dramatically influence the total hydrodynamic behavior of plasma through a radiation transport mechanism. This influence is discussed later, where Fig. 2 presents the calculated absorption coefficient with and without line splitting.

Another problem is that in ions with intermediate and high atomic numbers, some inner levels may have energies comparable to the ionization potential and the transitions from inner shells cannot be neglected. For example, in our situation of xenon plasma, where the major radiating wavelength region of interest is close to 13 nm, transitions from outer shells to $4d^q$ to $4d^{q-1}5p$ must be considered with transitions from the inner shells, say $4p^6 4d^q$ to $4p^5 4d^{q+1}$ and $4d^q$ to $4d^{q-1}4f$. Simplified methods may contain semiempirical information of atomic energy levels. Despite the fact that, for light elements, such tabulated information is sufficiently complete, for intermediate and high-Z elements it is usually incomplete.[9]

Generally, to accurately describe the atomic energy levels in xenon and other intermediate atoms, self-consistent Dirac-Fock or HF with relativistic corrections must be applied when the transition is calculated as the difference of total energies between levels. In practice, this procedure might be computationally intensive.

To calculate the structure of the atomic energy levels and the transition probabilities, the following procedure was applied by means of the HFS method, which gives one radial wave function for each shell of the atom. The obtained wave functions were used to calculate relativistic corrections, transition wavelengths, as well as dipole transitions from ground state to the highly excited state (principal quantum number may reach up to 10) allowed by the selection rules. Discrete transitions from inner shells were also taken into account, with energies limited to the value dependent on ionization potential. Photoionization cross sections were found for all inner and excited states. Details of these computations can be found elsewhere.[5,10] This procedure was repeated for the total ionization of the atom in question. The procedure of detailed accounting for spin-orbit splitting of nonfilled shells by using Slater integrals F^k, G^k, and constants of spin-orbit splitting ξ^k is implemented as given by Ref. 10.

It is known and has been thoroughly examined in several studies,[6,7] that radiative emission and transport plays a key role in the dynamics and energy balance of laboratory plasma. Recently, several studies[11,12] have shown that high-temperature, moderate-density plasma is not in local thermodynamic equilibrium and the radiative properties of plasmas that are optically thick to line radiation are not well-described by either ''coronal'' or Saha-Bolzmann models.

Normally, in the case of intermediate temperatures and densities, when collisional processes are still significant but, at the same time, radiative effects become apparent and cannot be negligible, it is necessary to solve the system of kinetic equations self-consistently with the radiation field. The model in self-consistent formulation takes into account nonlocal processes of photoexcitation and photoionization, and so, significantly complicates the computations. The problem becomes particularly difficult for high-Z plasma, because in evaluating the influence of external photons, it is necessary to account for a very large number of ionization and excitation levels.

This paper utilizes the description of atomic population levels by a CRE formulation, which is equally applicable to the limited cases of temperature and intermediate-temperature interval, because it includes, both collisional and radiative effects. The fact that the CRE model considers the transitions between all atomic levels is of particular importance. Nonlocal effects are accounted for by an escape factor approximation,[13] which neglects photoexcitation in continuum and reduces the strength of spontaneous transitions. Such an approximation is a fair description of the plasma behavior under conditions when an external source of hard radiation is absent.

The calculation of plasma ionization state and population levels n for a prescribed set of temperatures and densities is accomplished by solving the system of kinetic equations

$$\frac{dn_i}{dt} = -n_i \sum_{j \neq i} K_{ij} + \sum_{i \neq j} n_j K_{ji} . \tag{10}$$

Collisional electron excitation and deexcitation, collisional electron ionization, three-body recombination, spontaneous transition, photo- and dielectronic recombination are included in the calculation of the total rates of electron transition K_{ij} from level i to level j. Ion and electron concentrations N_i and N_e are defined from known population of levels for a given temperature and substituted into a set of equations of state. Generally, a two-temperature approximation for pressure p contains the corresponding terms for kinetic energy of ions and electrons. The equation for internal energy e_{int} contains the terms for ionization and excitation of electrons:

$$P = kT_i \sum_i N_i + kT_e N_e ,$$

$$e_{\text{int}} = \frac{3kT_e N_e}{2\rho} + \frac{3kT_i \Sigma_i N_i}{2\rho} + \frac{1}{\rho} \sum_i N_i \left[\left(\sum_{i-1} I_i \right) + \sum_j \frac{\varepsilon_{ji} N_{ji}}{N_i} \right]. \tag{11}$$

In our approximation, electron and ion temperatures are set equal, as $T_e = T_i = T$.

Reciprocal to the resistivity η, the electrical conductivity σ is found as the sum of scattering cross sections σ_c and σ_n on charged and neutral particles:

$$\eta = \frac{1}{\sigma} = \frac{1}{\sigma_c} + \frac{1}{\sigma_n}, \quad \sigma_c = \frac{4\sqrt{2}}{\pi\sqrt{\pi}} \frac{(kT_e)^{3/2}\beta}{e^2 Z \Lambda},$$

$$\sigma_n = \frac{3}{2} \left(\frac{2}{\pi} \right)^{1/2} \frac{N_e e^2}{(m_e kT_e)^{1/2} N_0 s_0}. \tag{12}$$

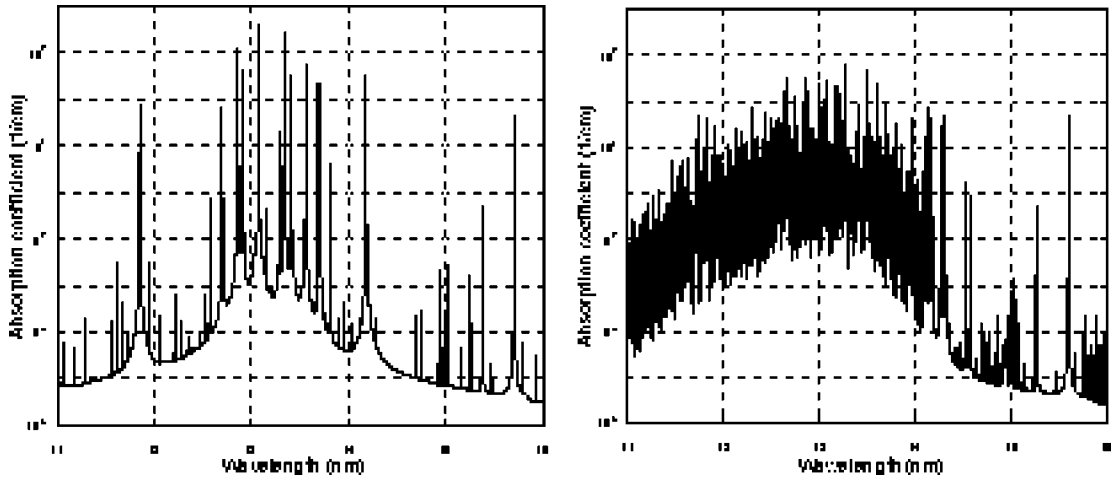

Fig. 2 Absorption of Xe plasma at temperature of 30 eV, density 10^{16} cm^{-3} with line splitting (right) and without splitting (left).

Here, we use standard notation for Coulomb log Λ, concentration of neutral atom N_0, and mean ion charge Z. Empirical values of transport cross sections s_0 are taken from Ref. 14.

Thermal conduction may be an important mechanism of energy redistribution in plasma in certain temperature regions until radiation becomes the dominating process.[15] Such a region is usually a weakly heated area with a low level of ionization, and consequently, with a low rate of collisional excitation. Depending on the temperature of the region, various effects may take place, and each may contribute its own part to the total energy balance. In a cold, weakly ionized gas, the classical approximation of dispersion of elastic spheres is the main energy redistribution mechanism, and the thermal conductivity χ_{el} depends on the average thermal velocity of the atom, and is proportional to $\sqrt{T}$. When temperature increases, dissociation becomes more important. When a molecule moves, the temperature on its path is changing and the concentration of molecules and neutral atoms is varying, and transferring energy equivalent to the value of the dissociation potential. Diffusion of neutral atoms to the weakly ionized plasma leads to energy transfer known as ambipolar diffusion. In intermediate levels of ionization, such neutral atoms would also ionize plasma and transfer energy. When the ionization level becomes significant, electron-ion dispersion dominates over other processes. We use all mentioned effects in our computation of thermal conductivity, except the process of ion-ion dispersion because so-called ''radiative thermal conduction'' is considered explicitly in the form of radiation transfer.

The electronic transitions and their accompanying absorption and emission of photons are subdivided into three types: bremsstrahlung; photoionization from ground, excited, and inner levels; and discrete transitions. The later are approximated in the form of dipole transitions and include transitions between ground and excited states, transitions between excited states, and partly, the transitions from inner shells. Because of its importance, the profiles of spectral lines is processed very carefully by means of all major broadening mechanisms such as radiation, Stark, Doppler, and resonance broadening.[16]

The total absorption coefficient κ_{abs} is calculated as a sum of absorption coefficients for, free-free κ_{ff}, bound-free κ_{bf}, and bound-bound κ_{bb} radiation transitions, weighted to the value of the population levels:

$$\kappa_{\mathrm{ff}}(T,\rho,\hbar\omega)=\sum_i \sigma_i(T,\hbar\omega)N_i(T,\rho)N_e(T,\rho) \times[1-\exp(-\hbar\omega/kT)],$$

$$\kappa_{\mathrm{bf}}(T,\rho,\hbar\omega)=\sum_i \sum_j \sigma_{ij}(\hbar\omega)N_{ij}(T,\rho), \tag{13}$$

$$\kappa_{\mathrm{bb}}(T,\rho,\hbar\omega)=\sum_i \sum_{j,k} \frac{\pi e^2}{m_e c} f_{jk}\Phi(T,\rho,\omega)N_{ij}(T,\rho).$$

Knowing the cross sections of inverse processes, we can calculate the total emission coefficient κ_{emi} by similar formulas. The values of oscillator strengths f_{jk}, cross sections for photoionization σ_{ij}, line profile Φ, and Gaunt factor G_i are explained in details elsewhere.[5,10,17]

Energy-level splitting produces a very complicated nonmonotonic dependence of the absorption coefficient on the frequency of incident photons. The importance of splitting was already discussed and is demonstrated in Fig. 2. To accurately describe the distinctions of the spectrum, the scale absorption frequencies must be detailed. In this study, we first generated 100,000 frequency points that are inconvenient for the practical solution of the multidimensional RTE. In solving the RTE, mean group coefficients are normally used when grouping does not have a strict algorithm and is defined by semiautomatic methods. The complexity of the choice of grouping methods is determined by the required accuracy of the computation, the frequency region of interest, and the available computer resources. Our study includes various algorithms of averaging by Planck and Rosseland and the number of spectral points may vary from tens to hundreds. A comparison of results calculated with various averaging methods, enables us to evaluate the sen-

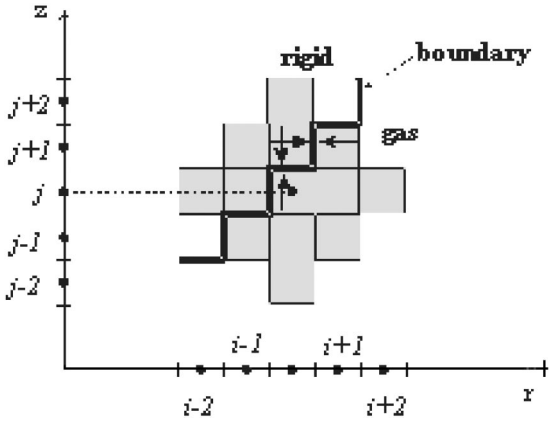

Fig. 3 Spatial discretization diagram and the system of boundary conditions.

sitivity of the calculations to the spectral choice, whereas convergence of the radiation flux by the number of groups estimates the accuracy of the computation.

5 Numerical Method

The HEIGHTS-EUV is subdivided into several major parts: (1) the geometrical and configuration parameters; (2) initial plasma state, hydrodynamic mesh, and plasma parameters, stated in the block, which calculates MHD motion of the plasma; (3) atomic parameters, and (4) radiation transport parameters. The TVD-LF algorithm, implemented in HEIGHTS-EUV, is a second-order monotonic-upwind-schemes-for-conservation law (MUSCL). The discrete approximation is carried out by a central finite-difference scheme, schematically shown in Fig. 3. The Hancock predictor step[18] is implemented because it is superior to the simple Euler transport step:

$$U_{i,j}^{n+1/2}=U_i^n-\frac{\Delta t^n}{2r_i\Delta r_i}[r_{i+1/2}F(U_{i+1/2,j}^n)-r_{i-1/2}F(U_{i-1/2}^n)]-\frac{\Delta t^n}{2\Delta r_i}[P(U_{i+1/2,j}^n)-P(U_{i-1/2,j}^n)]-\frac{\Delta t^n}{2\Delta z_i}[G(U_{i,j+1/2}^n)-G(U_{i,j-1/2}^n)]+\frac{\Delta t}{2}\Omega_{i,j}. \tag{14}$$

The values of U at cell borders $U_{i\pm1/2,j}^n=U_{i,j}^n\pm(1/2)\overline{\Delta U_{i,j}^r}$ are calculated from the limited differences $\overline{\Delta U_{i,j}^r}$.

The described method for linear approximation of solution U and the corresponding fluxes at boundary interfaces achieve second-order accuracy in spatial discretization. HEIGHTS-EUV may generate limited differences by using four types of slope limiters: simple minmod, UMIST, Woodward, and superbee, described in detail by Ref. 18. Sufficient stable test results were obtained by using the simple minmod limiter:

$$\overline{\Delta U_{i,j}^r}=\mathrm{minmod}(\Delta U_{i-1/2,j}^n,\Delta U_{i+1/2,j}^n)=\mathrm{sgn}(\Delta U_{i-1/2,j}^n)\max\{0,\min[|\Delta U_{i-1/2,j}^n|,\mathrm{sgn}(\Delta U_{i-1/2,j}^n)\cdot\Delta U_{i+1/2,j}^n]\}. \tag{15}$$

The corrector step includes the final limiter function $\tilde{F}_{i+1/2,j}^{LR}$, which contains predictor data and a maximal propagation speed of information $c_i^{\max}=|v_i|+[v_{ac}^2+(B^2/4\pi\rho)]^{1/2}$, where v_i is gas velocity in the i direction, and v_{ac} stands for the velocity of sound.

$$\tilde{F}_{i+1/2,j}^{LR}=\frac{\Delta t^n}{0.5(\Delta r_i+\Delta r_{i+1})}c_{i+1/2,j}^{LR}\Delta U_{i+1/2,j}^{LR},$$

$$\Delta U_{i+1/2,j}^{LR}=U_{i+1/2,j}^R-U_{i+1/2,j}^L,$$

$$U_{i+1/2,j}^L=U_{i,j}^{n+1/2}+\frac{1}{2}\overline{\Delta U_{i,j}^r},$$

$$U_{i+1/2,j}^R=U_{i+1,j}^{n+1/2}-\frac{1}{2}\overline{\Delta U_{i+1,j}^r}. \tag{16}$$

The final expression for the TVD solution at the $n+1$ time step is given by

$$U_{i,j}^{n+1}=U_{i,j}^n-\frac{\Delta t^n}{r_i\Delta r_i}(r_{i+1/2}F_{i+1/2,j}^{LR}-r_{i-1/2}F_{i-1/2,j}^{LR})-\frac{\Delta t^n}{\Delta r_i}(P_{i+1/2,j}^{LR}-P_{i-1/2,j}^{LR})-\frac{\Delta t^n}{\Delta z_j}(G_{i,j+1/2}^{LR}-G_{i,j-1/2}^{LR})+\frac{1}{2}(\tilde{F}_{i+1/2,j}^{LR}-\tilde{F}_{i-1/2,j}^{LR})+\frac{1}{2}(\tilde{G}_{i,j+1/2}^{LR}-\tilde{G}_{i,j-1/2}^{LR})+\Delta t^n\Omega_{i,j}. \tag{17}$$

Analysis of a TVD-LF scheme shows that the total solution of the MHD equations with TVD corrections enables componentwise decomposition. We used this property to elaborate the method of setting up boundary conditions and avoiding either introducing coordinate charts or implementing ''fractional'' mesh cells (Fig. 3).

The radiation transport part is implemented separately because it requires significant computational resources. The formal solution of the RTE [Eq. (8)] is readily written as

$$I_E(s)=I(0)\exp[-\tau(s,0)]+\int_0^s B_E\exp[-\tau(s,s')]\times\kappa_{\mathrm{abs}}\rho\,ds', \tag{18}$$

which expresses the fact that the intensity at any point and in a given direction is the result of the emission at all anterior points s', reduced by the factor $\exp[-\tau(s,s')]$ to allow for absorption by intervening matter where τ, is the optical thickness, of the material between points s and s'.

The values of intensity are calculated in the bounds of the hydrodynamic mesh cells, whereas optical characteristics, defined by temperature and density, are calculated by

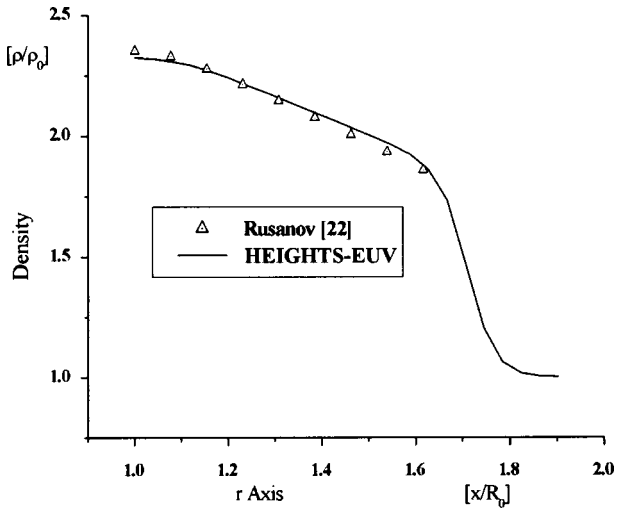

Fig. 4 Shock wave pressure from 1.5 M flow around a sphere.

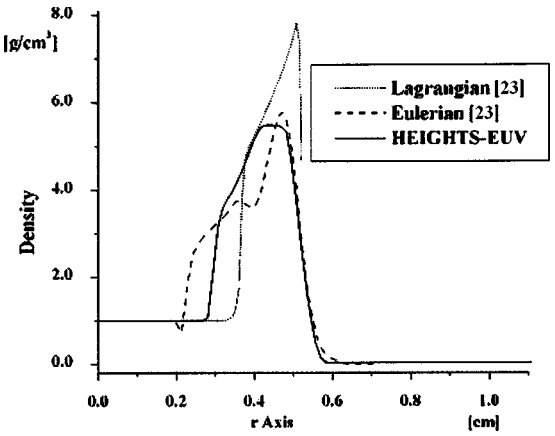

Fig. 5 Z-pinch at 0.49 s.

mean values in center points of the cells. Integration over spectral groups is performed to obtain the total flux at central points of hydrodynamic cells, where spectral intervals are given by boundary values. Because the discrete-ordinates algorithms allow photon streaming only in prescribed directions, the low-order quadrature is unable to accurately approximate the scalar flux by integrating over the angular flux and can exhibit nonphysical oscillations, because regions lying between the directions are not covered by photons emanating from the source. Mesh refinement or increased order of angular quadrature may only mitigate the effect. In a critical situation, when such a ray effect must be eliminated, a set of coupled transport equations, invariant under discrete rotations, may help.[19] In our study, an extremely high order (up to 96) Gaussian quadrature is used[20] to integrate over angles φ, and θ [Eq. (9)], that give a direction of the ray. Plain geometrical construction and the use of cylindrical symmetry enable the coupling 3-D radiation transport resolution into 2-D MHD space.

Because of the large number of rays, the computation rate may escalate to a high level, even if the spatial mesh order is not very large. Parallel computers are traditionally used to speed up an application. The resolution of RTE is implemented as a parallel message passing interface procedure,[21] enabling a gain by simultaneously calculating the net fluxes $\mathbf{S}_{\text{rad}}$ at several spatial points. An unsophisticated algorithm of load balancing is activated to dynamically distribute the amount of work according to the processor speed that makes possible the utilization of homogeneous as well as heterogeneous clusters of workstations.

6 Validation and Benchmarks

To validate the MHD models and benchmarking of the code, two test problems were solved and compared with known results. The first test problem is described in detail in Ref. 22, where studies of a supersonic flow around a sphere without a surrounding magnetic field are discussed. The results reported in Ref. 22 and those numerically calculated by HEIGHTS-EUV are shown in Fig. 4. We see from the figure that our computation almost exactly repeats the tabulated density distribution along the radial axis. The second test consisted of resolving the dynamic of one-dimensional Z-pinch, and comparing the results with those reported in Ref. 23, in which implementation of several MHD schemes related to a pinch problem are reported. We compared our TVD-LF scheme with magnetic field to Lagrangian and Eulerian formulations. The results of Z-pinch simulations are presented in Fig. 5. As one can see, our implementation is a satisfactory trade-off between Eulerian and Lagrangian schemes. The density curve does not have the nonphysical oscillations seen in results obtained by the Eulerian method. Despite the fact that HEIGHTS-EUV does not isolate the shock front as the Lagrangian scheme does, our simulation package does not have the difficulties known to the mesh cells, which would inevitably appear in the Lagrangian formulation at the moment of the pinch collapse.

Figures 6 and 7 show the preliminary results of a DPF discharge as simulated by the HEIGHTS-EUV package. The results shown are near the moment of plasma pinching. The absolute values of the density and temperature depend on the detailed physics of the discharge as well as on the electric circuit design and the current profile. The maximum radiation is emitted near regions of temperature below 40 eV. Future analysis will study the effect of initial gas pressure, preionization channels, and electric current profile on the overall performance and efficiency of the discharge.

7 Conclusions

We presented an integrated model that is being developed to describe the hydrodynamics and optical processes that occur in DPP devices. The model addressed three main subjects: plasma evolution and MHD processes, detailed photon radiation transport, and interaction between plasma/radiation and material. The developed models and numerical methods are being implemented and integrated in the computer simulation package HEIGHTS-EUV. The package, when completed, will be a tool that can be used to study, optimize, and enhance our understanding of the MHDs and radiation processes in DPP devices and the issues related to component erosion and lifetime estimates.

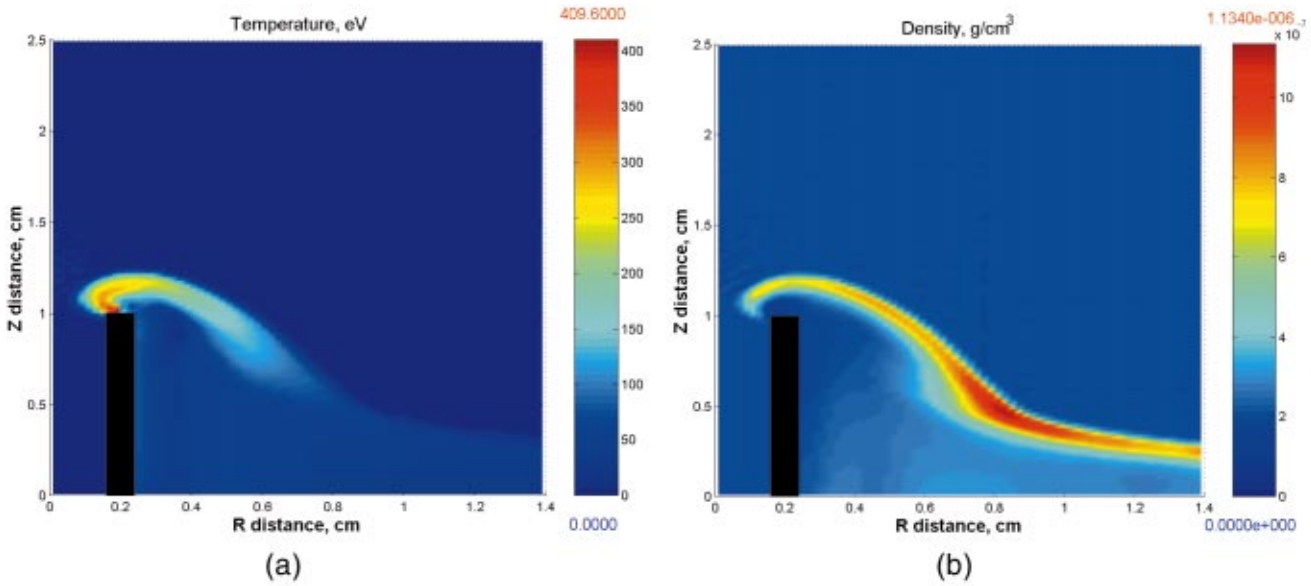

Fig. 6 Temperature and density distribution close to pinching time.

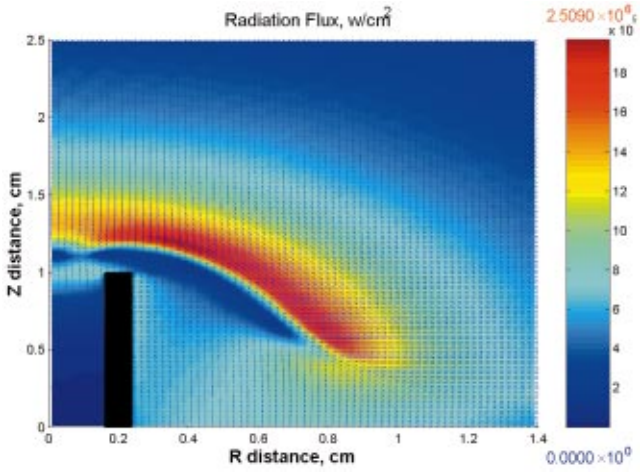

Fig. 7 Radiation flux near pinching time.

Acknowledgments

The submitted manuscript has been created by the University of Chicago as Operator of Argonne National Laboratory (''Argonne'') under Contract No. W-31-109-ENG-38 with the U.S. Department of Energy. The Intel Corporation supported a major portion of this work.

References

1. G. Tóth, ''The $\nabla \cdot B = 0$ constraint in shock-capturing magnetohydrodynamics codes,'' *J. Comput. Phys.* **161**, 605–652 (2000).
2. R. Siegel and J. R. Howell, *Thermal Radiation Heat Transfer*, 3rd ed., Hemisphere, Washington, DC (1994).
3. B. G. Carlson, ''Solution of the transport equation by S_n approximations,'' Los Alamos National Laboratory, Report LA-1599 (1953).
4. S. Chandrasekhar, *Radiative Transfer*, Dover, New York (1960).
5. V. Tolkach, A. Hassanein, and V. Morozov, ''Development of comprehensive models for opacities and radiation transport for IFE system,'' Argonne National Laboratory, Report ANL-ET/02-23 (2002).
6. I. N. Burdonskii et al., ''Experimental, numerical, and theoretical studies of x-radiation and radiative thermal conductivity in a dense laser plasma with multicharged ions,'' *JETP* **79**, 879 (1994).
7. B. N. Bazylev et al., ''Investigation of energy transfer in plane laser-irradiated targets with high x-ray conversion efficiency,'' *Laser Part. Beams* **12**(3), 355 (1994).
8. J. C. Slater, ''A simplification of the Hartree-Fock method,'' *Phys. Rev.* **81**, 385 (1951).
9. C. E. Moore, ''Atomic energy levels as derived from the analyses of optical spectra,'' National Bureau of Standards NSRDS-NBS 35 (1971).
10. I. I. Sobelman, *Introduction to the Theory of Atomic Spectra*, Pergamon Press, Oxford, NY (1972).
11. J. J. MacFarlane and P. Wang, *Phys. Fluids* **B3**, 3494 (1991).
12. J. J. MacFarlane et al., *Fusion Technol.* **26**, 886 (1994).
13. T. Holstein, ''Imprisonment of resonance radiation in gases,'' *Phys. Rev.* **72**(12), 1212 (1947).
14. L. Huxley and R. Crompton, *The Diffusion and Drift of Electrons in Gases*, Wiley Woodhouse, NY (1974).
15. L. Spitzer, *Physics of Fully Ionized Gases*, 2nd ed, Interscience, New York (1962).
16. H. R. Griem, *Spectral Line Broadening by Plasmas*, Academic Press, New York (1974).
17. I. I. Sobelman, L. A. Vainshtein, and E. A. Yukov, *Excitation of Atoms and Broadening of Spectral Lines*, Springer-Verlag, Berlin, New York (1981).
18. G. Tóth and D. Odstrcil, ''Comparison of some flux corrected transport and total variation diminishing numerical schemes for hydrodynamic and magnetohydrodynamic problems,'' *J. Comput. Phys.* **128**, (1996).
19. R. T. Ackroyd, *Finite Element Methods for Particle Transport, Applications to Reactor and Radiation Physics*, Research Studies Press, (1997).
20. M. Abramowitz and I. Stegun, *Handbook of Math. Functions*, Dover, New York (1965).
21. M. Snir et al., *MPI—The Complete Reference*, MIT Press, Cambridge, MA (1998).
22. A. N. Lubimov and V. V. Rusanov, *Gas Flows around Obtuse Bodies, Part I. Calculation Method and Analysis of Flows, Part II, Tables of Gas Dynamic Functions* Moscow (1970).
23. A. G. Axenov and A. V. Gerusov, ''Comparison of numerical calculation methods of two-dimensional MHD flows with high compression,'' *Plasma Phys.* **21**, 1 (1995) (in Russian).

Biographies and photographs of the authors not available.